Computational and Structural Biotechnology Journal
A SCIENCE PARTNER JOURNAL

RESEARCH ARTICLE

The Redesign of the Molecular Scaffold of Viral Ion Channel Blockers

Balázs Zoltán Zsidó[1], Erzsébet Mernyák[2], Zoltán Kopasz[3,4], Fanni Földes[3], Krisztina Leiner[3,4], Mónika Madai[3], Brigitta Zana[3], Anett Kuczmog[3,4*], and Csaba Hetényi[1*]

[1]Pharmacoinformatics Unit, Department of Pharmacology and Pharmacotherapy, Medical School, University of Pécs, 7624 Pécs, Hungary. [2]Institute of Pharmacognosy, University of Szeged, H-6720 Szeged, Hungary. [3]National Laboratory of Virology, Szentágothai Research Centre, University of Pécs, 7624 Pécs, Hungary. [4]Institute of Biology, Faculty of Sciences, University of Pécs, 7624 Pécs, Hungary.

*Address correspondence to: kuczmog.anett@pte.hu (A.K.); hetenyi.csaba@pte.hu (C.H.)

Citation: Zsidó BZ, Mernyák E, Kopasz Z, Földes F, Leiner K, Madai M, Zana B, Kuczmog A, Hetényi C. The Redesign of the Molecular Scaffold of Viral Ion Channel Blockers. *Comput. Struct. Biotechnol. J.* 2026;35(1):Article 0188. https://doi.org/10.34133/csbj.0188

Submitted 18 May 2026
Revised 10 July 2026
Accepted 13 July 2026
Published 3 August 2026

The rise of rapidly mutating viruses poses growing challenges for drug developers in the fight against antiviral resistance. Viral ion channels generally have low mutation rates and are therefore considered emerging targets for a sustainable solution to the problem of resistance. This study reports the redesign of scaffolds for drug candidates targeting viral ion channels. The redesign was powered by a combination of a computational docking protocol that accounts for water molecules (HydroDock) and a subsequent quantum mechanics-based scoring (QMH-L) of the drug candidates. Extending the antiviral amantadine led to new compounds that better match the alternating hydrophobic and hydrophilic patterns of the inner walls of ion channels—a common feature across many viruses. Simplifying the structure yielded a cyclohexylamine-based minimalist scaffold that demonstrates improved antiviral activity compared to other agents such as amantadine and arterolane. SARS-CoV-2 variants served as test systems in laboratory experiments. The new molecular scaffolds presented here provide a strong foundation for designing potent viral ion channel blockers, helping to fill the drug pipeline.

Introduction

Antiviral design is hindered by a lack of reliable animal models and a scarcity of conserved targets [1–3] within the small viral proteome [4]. While enzymes are common viral targets [5,6], frequent mutations in their binding pockets ([7–9]; Fig. S1) lead to the rapid evolution of antiviral resistance [10–12]. The low binding affinity [13,14] and narrow spectrum [14,15] of enzyme inhibitors limit their utility as drugs. As seen with nirmatrelvir, even Food and Drug Administration (FDA)-approved drugs with strong *in vitro* activity [16] can fail to prevent viral reemergence [17], as the virus quickly develops resistance [7,8,18–21] through target mutations [7,8,18–22].

Targeting proteins other than enzymes, particularly ion channels [23,24] offers a strategy to overcome the antiviral challenges [25] outlined above. Viral ion channels are often conserved (Fig. 1A) or possess only a few mutations that are deleterious and prevent viral replication [26–28], and therefore they are emerging targets in the fight against antiviral resistance. The internal structure of viral ion channels often features an alternating pattern of hydrophilic and hydrophobic bands (Fig. 2). They can accommodate [29] not only ions but also small drug molecules such as amantadine (AMA) and rimantadine (RIM, Fig. 1B). AMA and RIM were initially approved for the treatment of influenza A [30]. Such ion channel blockers with an amphiphilic scaffold (AMS) are composed of a hydrophilic head (the protonated amino group [30]) and a hydrophobic tail (the bulky adamantyl group [31]; Fig. 1B). This chemical match between AMSs and the alternating pattern of ion channel interiors results in an efficient block of ion transport [29,32] and disruption of viral replication [32]. The development of AMS antivirals is promising for at least 3 main reasons.

1. Known AMS compounds primarily block conserved viral ion channels, such as the M2 protein of influenza A [30] and the envelope protein (EP) of SARS-CoV-2 [32,33], which are promising drug targets in the long term. For example, EP is less mutagenic ([27,34–36]; Fig. 1A) than other SARS-CoV-2 proteins, such as the spike protein (Fig. S1), which is primarily responsible for vaccine resistance [22].
2. In an AMS, a bulky hydrophobic tail can shield the hydrophilic head from metabolic cleavage by limiting the access of metabolic enzymes [31,37]. That is, the electron-rich adamantane tail can be hydroxylated by CYP450 enzymes [38] instead of the head of AMS.
3. The AMS compounds are potent antivirals due to their target similarity. They have been effective against various viruses, including influenza A [39], SARS-CoV-1 (with an almost identical EP sequence [40,41]), SARS-CoV-2 [29,32,42–46], and hepatitis A [47]. The AMS pattern fits the alternating hydrophilic and hydrophobic bands

A

```
Alpha   (OR584241.1)MYSFVSEETGTLIVNSVLLFLAFVVFLLVTLAILTALRLCAYCCNIVNVSLVKPSFYVYSRVKNLNSSRVPDLLV
Delta   (PV848452.1)MYSFVSEETGTLIVNSVLLFLAFVVFLLVTLAILTALRLCAYCCNIVNVSLVKPSFYVYSRVKNLNSSRVPDLLV
Omicron (OP183454.1)MYSFVSEETGTLIVNSVLLFLAFVVFLLVTLAILTALRLCAYCCNIVNVSLVKPSFYVYSRVKNLNSSRVPDLLV
Wuhan   (NC_045512) MYSFVSEETGTLIVNSVLLFLAFVVFLLVTLAILTALRLCAYCCNIVNVSLVKPSFYVYSRVKNLNSSRVPDLLV
                    ************************************************************************
```

B

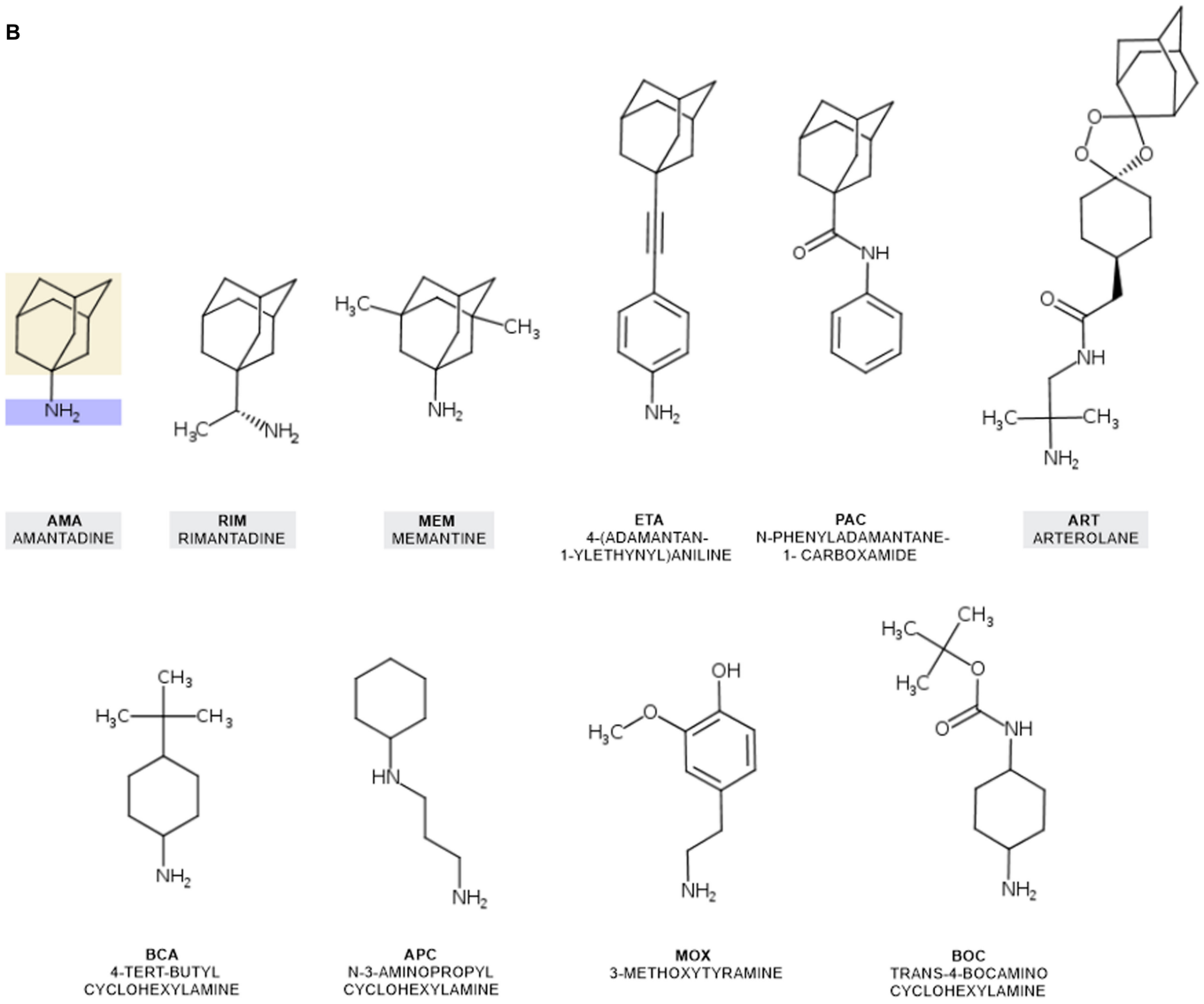

Fig. 1. (A) The amino acid sequence alignment of the envelope protein (EP), the ion channel of SARS-CoV-2, shows no mutations between the different variants. Sequences were obtained from the National Center for Biotechnology Information [101], with repository codes shown in the figure. The transmembrane region is colored gray [32]. Sequence alignment was performed using Clustal Omega [102]. Positions with identical amino acids are marked with asterisks. (B) The compounds with an amphiphilic scaffold (AMS) investigated in the present study are arranged in increasing order of molecular weight. The compounds in the upper row are based on the AMA scaffold, while those in the lower row have a simplified (minimalist) scaffold. The labels of FDA-approved drugs (used as references) are highlighted in gray. The AMS, composed of a hydrophobic (sandy background) and hydrophilic (blue background) group, is highlighted in AMA.

(Fig. 2) of the inner wall of ion channels present in different viruses [32], allowing broad repurposing.

Given the structural similarity (Point 3) of the targeted ion channels, it was possible to reposition the AMS compounds from M2 of influenza to EP of SARS-CoV-2. This repositioning was first suggested by a nuclear magnetic resonance (NMR) study [32] and later supported by *in vitro* and *in vivo* studies [32,42–46] and several clinical trials and clinical case studies [48–54]. The initial insights into how AMA-based compounds bind to EP were provided by NMR [32] and *in silico* [29] studies. Later, several electrophysiology studies verified that the EP is the target of the AMS compounds in SARS-CoV-2 [55–59].

Recently, 5 *in silico* studies were published on SARS-CoV-2 [41,60], Ebola virus [61], and protein folding and compound classification [62,63]. Three combined *in silico/in vitro* studies were published on influenza A virus [64] and *Clostridium* bacterium

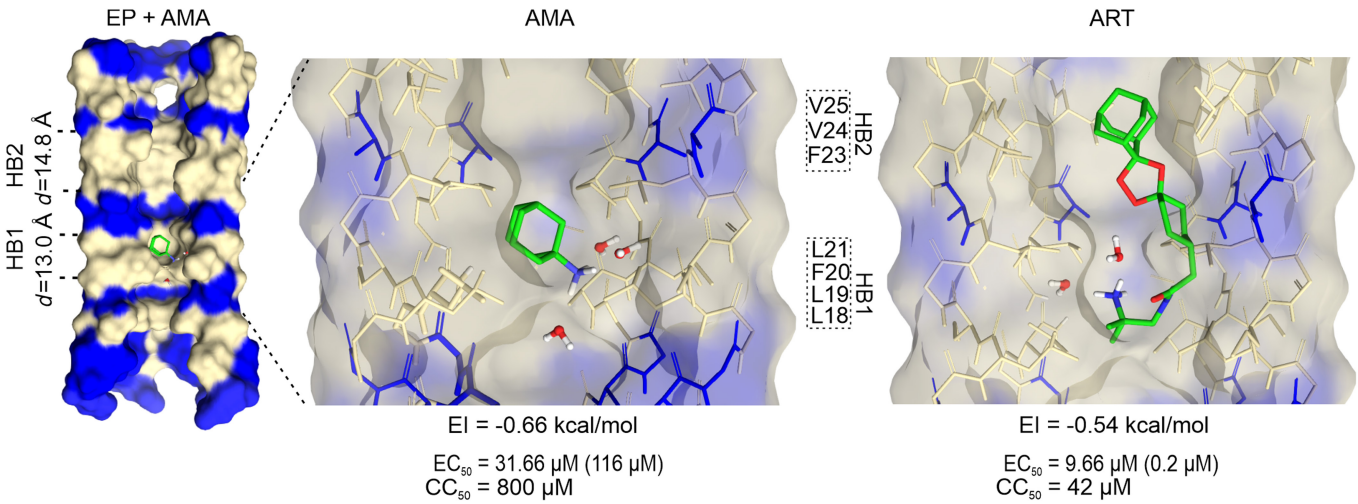

Fig. 2. The ion channel (EP) of SARS-CoV-2 binding AMS compounds. Cross-section of EP shown as a surface (left), with AMA (middle), and arterolane (ART) (right) represented with sticks. The blue and tan bands indicate hydrophilic and hydrophobic regions, respectively, based on the chemical properties of the amino acid residues lining the internal wall of EP. The hydrophobic adamantyl group of AMA fits into the hydrophobic bands of EP, while the hydrophilic amino group interacts with the hydrophilic bands via water molecules. These bridging water molecules are represented as red and white balls-and-sticks (not all are shown for clarity). Amino acids are labeled according to PDB entry 7k3g [32]. Hydrophobic bands (HBs) 1 and 2 are labeled, with their diameters shown, and the amino acids highlighted within each HB. The bottom of the figure points toward the extraviral space. Antiviral activity against the alpha variant in the present study is shown (measured by MTT assay), and literature activity values [46,82] are in brackets. Cytotoxicity values are also from the present manuscript.

[65] and TRPV2 receptor [66] with methods similar to those used in our study.

While the examples above show a promising direction, the number of studies reporting new AMSs is limited by several issues. A detailed structure–activity relationship (SAR) elucidation and computational technology are needed (see the author's remark in Ref. [43]) to sustain rational target-based AMS design. For viruses like SARS-CoV-2, laboratories with high safety standards at Biological Safety Level 3 (BSL-3; [67]) are necessary to test the antiviral potency of new AMS. Testing of AMS compounds across different variants is completely missing. Furthermore, the synthetic challenges [68] of adamantyl derivatives (Fig. 1B) also hinder the design of new AMS compounds. The present study addresses these issues and introduces a combination of computational techniques resulting in new compounds with an extended, then simplified, synthetically feasible AMS. Their antiviral activity and safety were tested against various SARS-CoV-2 variants in a BSL-4 laboratory.

Results and Discussion

The rethinking of AMS design was carried out through a 4-step process in this study. It started with building and validating SARs for known AMS compounds (Step 1). This involved identifying atomic resolution binding modes and calculating their binding affinities. After successfully repositioning M2 to EP, valuable M2-binding and affinity data were also integrated into the SAR development. Experimental test systems were established to verify the virological and cytological activity of the AMS shown in Fig. 1B (Step 2). Using the SARs from Step 1, the AMA scaffold was expanded (Step 3) to better match the ion channel. Finally, simplification (Step 4) resulted in a new, broadly applicable scaffold. In the following sections, Steps 1 to 4 will be described in detail.

Building and validation of SARS

Drug design requires precise SARs based on atomic-resolution structures, but experimental data are currently limited to the influenza M2 channel in complex with AMS compounds [30]. In the case of SARS-CoV-2, only the structure of the unliganded (apo) EP was measured [32] and an *in silico* study [29] explored the binding modes of AMA and RIM to EP using a new protocol, HydroDock [29], that accounts for interacting water molecules that are often crucial in drug binding [69,70] to ion channels [71]. The MD step of HydroDock uses explicit water molecules, which are necessary to stabilize ligand binding to the hydrophobic interior environment of EP. Docking without water molecules was found to fail to reproduce experimental ligand-binding modes to the viral ion channel of influenza A [29], and the inclusion of an MD step in the protocol improved ligand-binding modes via a network of interacting water molecules [29]. The binding modes of other compounds in Fig. 1B, including the new candidates, were also calculated by HydroDock in the present study. The first step of HydroDock is blind docking [72], which explores all possible binding modes of the compounds on the entire surface of the target protein. Binding to the N-terminal vestibule (T11, N15, and L18 amino acids) and the interior of EP is detailed in our previous study [29]. Binding to both N- and C-terminal vestibules are detailed in another study [73]. In agreement with the NMR findings [32], binding modes inside the ion channel were considered in the present study. The binding modes were piped into and scored by the quantum mechanics-based QMH-L [69] method. QMH-L calculates binding free energies (ΔG_b; Table S1) and is particularly effective [74,75] because it accounts for the electronic effects that have a considerable contribution to energy changes due to the large dipole moment of water molecules [70,71,76]. QMH-L had been originally validated [69] on a diverse set of 43 target–ligand complexes. In the present study, validation was extended to the available M2 and EP complexes with known activity, and a strong correlation (R^2 = 0.88, RMSE = 0.73 kcal/mol; Fig. 3A) was observed between the QMH-L-calculated ΔG_b values and experimental pEC_{50} (logarithm of the 50% effective concentration).

Similarly, a strong correlation (Fig. 3B) was observed for the calculated efficiency index (EI = ΔG_b/NHA, where NHA is the

number of heavy atoms [77] in the AMS compound) values. EI is a key metric recommended for scaffold design [77]. Experimental EI was calculated from pEC_{50} (instead of ΔG_b in the numerator) and reflects per-atom binding strength (activity) [78]. Along with previous validations [29,69], the results in Fig. 3 show that, beyond their general applicability, the computational tools HydroDock and QMH-L are reliable for designing antivirals, particularly targeting ion channels such as EP.

A co-analysis of the ΔG_b values with the corresponding experimental and/or HydroDock-based structures showed that the binding of AMS compounds is weaker to EP than to M2 (Fig. S2). Since the hydrophobic band (HB1; Fig. 2) of EP is wider than that of M2, small molecules like AMA or RIM, which fit perfectly to M2, fail to fill the larger space in EP, resulting in a weaker binding (Table S1) and lower antiviral activity against SARS-CoV-2 (Table S2). Among the tested FDA-approved AMS drugs, arterolane (ART), a repositioned anti-malaria [79] drug, has the most negative ΔG_b and the strongest binding to EP (Table S1) because its larger scaffold spans both HB1 and HB2 (Fig. 2), leading to the most potent antiviral activity (50% effective concentration [EC_{50}] = 9.66 μM; Table S3 and Fig. 2). However, the amide and amino groups in ART are also positioned in HB1 (Fig. 2), which makes having these hydrophilic groups in this hydrophobic environment energetically unfavorable. HydroDock calculations (Fig. 2) also showed that 3 water molecules occupying the HB1 space around the amino group stabilize ART's binding to EP, even in this unfavorable environment.

Based on the SAR results above from Step 1, we concluded that extending the AMS along the vertical axis of the ion channel improves binding strength and antiviral activity only if the extension does not merely fill empty cavities in EP. The extension only makes sense if the AMS interacts with consecutive hydrophobic and hydrophilic bands (as ART in Fig. 2) and water molecules inside EP.

Virology and cytology laboratory verification setup

As a further preparation for verifying the new AMS compounds (introduced in the next Steps 3 and 4), virology and cytology laboratory experiments (Fig. 4) were set up and tested with the known drugs listed in Fig. 1 (gray). Robust colorimetric assays [80,81] were used to experimentally verify the antiviral activity (blocking of *in vitro* viral replication) of all AMS (Fig. 1B) predicted by the computational design. The antiviral activities of AMS were expressed as the EC_{50}, a widely used measure in the literature [46,82–84]. The assays can readily measure the inhibition of viral cytopathic effect by AMS against various SARS-CoV-2 variants, as shown for the example of ART (Fig. 4A). The experimental effect can be followed in a series of representative microscopic images of Vero E6 cell cultures (Fig. 4B). 3-(4,5-Dimethylthiazol-2-yl)-2,5-diphenyltetrazolium bromide (MTT) assays were used for the EC_{50} measurements, where a considerable difference was observed among the baseline viability of healthy cells, the AMS-treated cells, and the infected cells.

Similarly, the Vero E6 cell line was also used to determine the 50% cytotoxic concentration (CC_{50}). AMA was found to be the least toxic (highest CC_{50}; Fig. 2 and Table S3), while ART is the most toxic (Fig. 2) among the 4 drugs (Fig. 1B) used as references in this study. The CC_{50} values for the 4 reference drugs closely align with data from previous research ($R^2 = 0.98$; Table S2 and Fig. S3). Overall, our virology and cytology laboratory experiments are consistent with previous laboratory protocols and results for the reference drugs and provide a reliable testing platform for the new compounds introduced in the next steps.

Extension of the AMA scaffold

Building on the previous SAR findings (Step 1), the AMS was redesigned to reduce issues related to the chemical synthesis, accessibility, and cost of spiro-compounds like ART and spiro-adamantyl amine (SPA; [29]; Fig. S4), while also improving the binding of the base compound AMA to EP. (At the time of

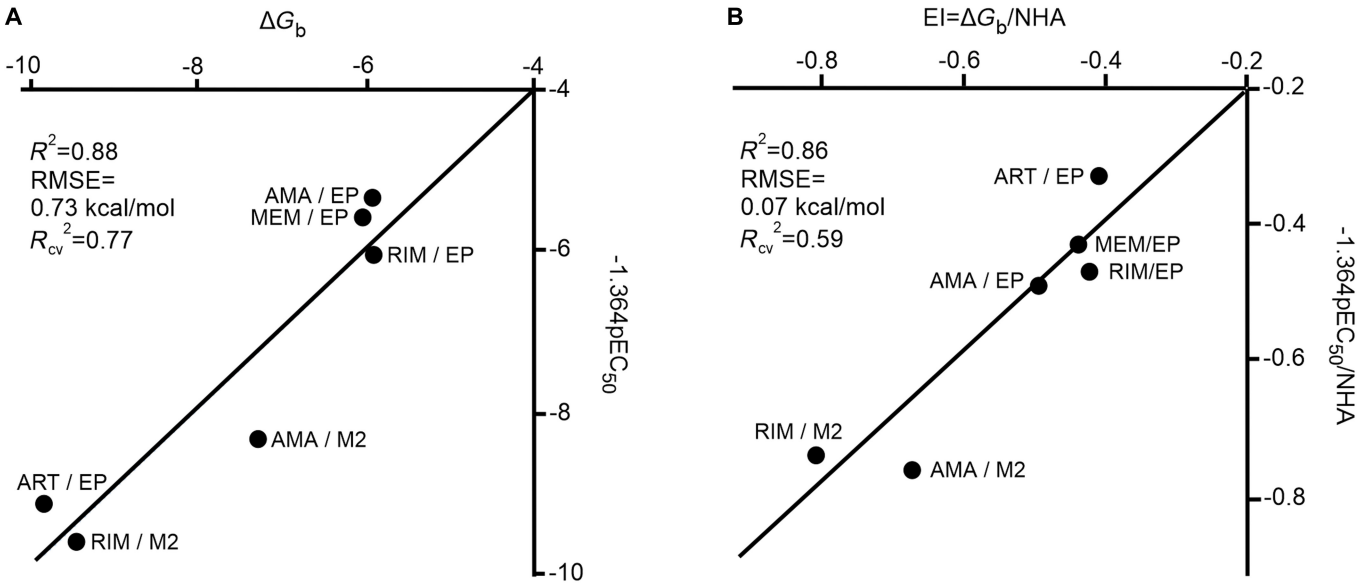

Fig. 3. The validation of the QMH-L binding affinity calculations based on complex structures of AMS compounds and ion channels M2 and EP generated by HydroDock in the previous [29] and the present study (Methods). (A) The correlation plot of experimental antiviral activity (pEC_{50}) and calculated binding affinity (ΔG_b, kcal/mol) is based on experimental EC_{50} data (Table S2) from the literature and QMH-L calculated values (Table S1) of the present study. (B) The correlation plot was also produced for the calculated EI (kcal/mol) values. The coefficient −1.364 comes from converting pEC_{50} to ΔG_b using the equation $\Delta G_b = RT \ln EC_{50}$, where R is the gas constant and $T = 298.15$ K is the temperature. The points are labeled according to drug/target.

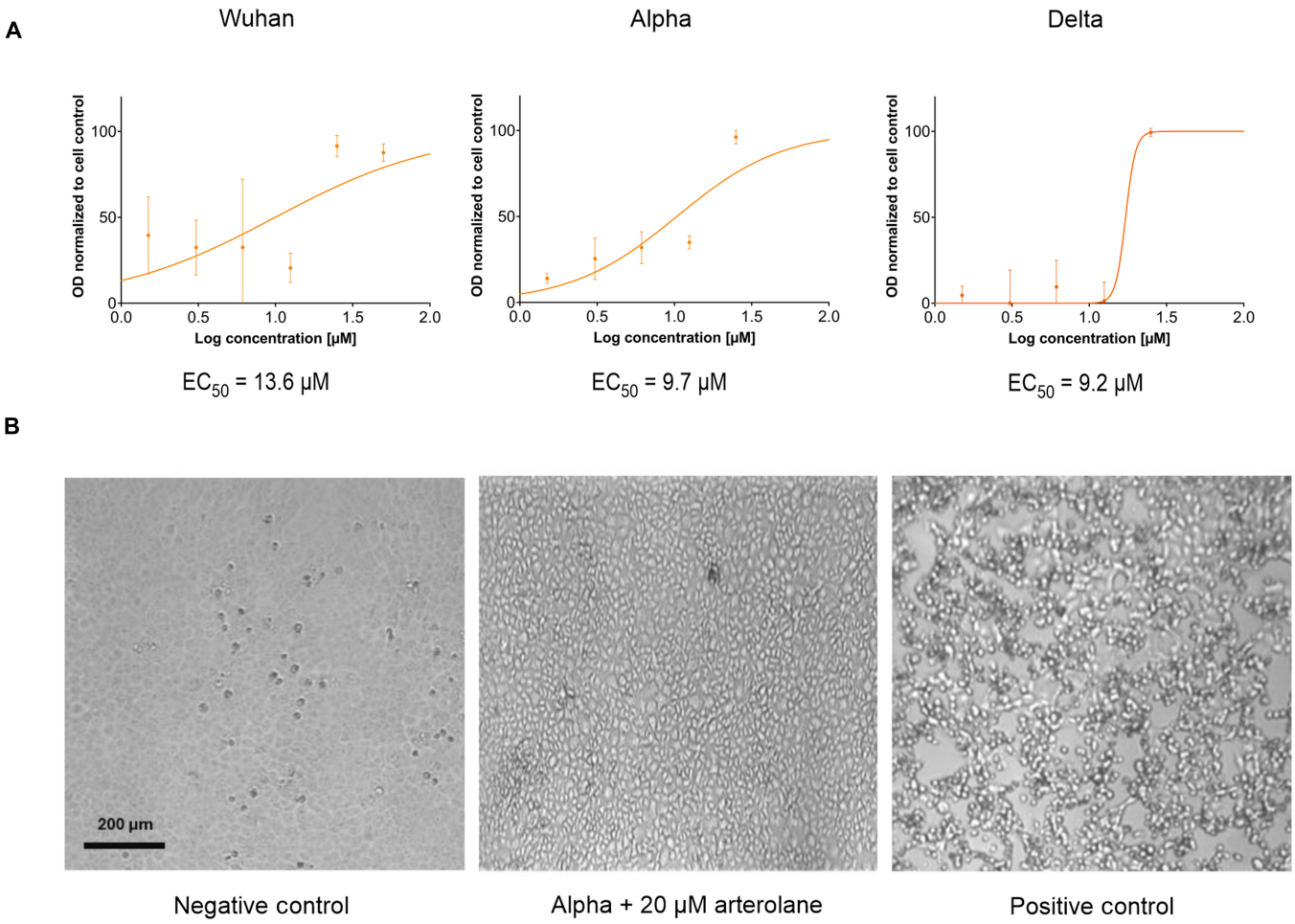

Fig. 4. ART inhibits SARS-CoV-2 replication *in vitro*. (A) Wuhan, alpha, and delta strain-infected (labeled accordingly) cells were treated with ART. The concentration–response curves were generated from a representative biological experiment, in which each concentration was measured in 3 technical replicates. A sigmoid curve is fitted to the measured optical density data from MTT assays. The standard error of measurement of 3 replicates is shown with error bars. (B) Representative microscopy images show antiviral activity. The microscopy images illustrate the cytotoxic effects of viral infection and their reversal by arterolane treatment. Granule-like appearances indicate cell death.

preparing this study, ART was purchased at a very high price, and SPA was not available on the market.) To achieve this, the adamantyl ring of AMA was extended with a small linker and a (substituted) phenyl group (Fig. 5 and Fig. S4) instead of the spiro-system. This redesign produced 2 new AMS with an extended scaffold: *N*-phenyladamantane-1-carboxamide (PAC; Fig. 1B) and 4-(adamantan-1-ylethynyl)aniline (ETA; Figs. 1B and 5), each featuring a different linker (amide and ethynyl, respectively).

HydroDock modeling shows that these rigid, linear molecules are perfectly sized to span both the HB1 and HB2 regions of EP (Fig. 6). The geometric design eliminated the problematic contacts (Fig. 2) involving the amide and amino groups of ART. While PAC also contains an amide group in the middle, it interacts with the hydrophilic band and a water molecule (Fig. 6A). The amino group of ETA binds to another water molecule within the hydrophilic band of EP, above HB 1. The phenyl groups of PAC and ETA bind to L18 and L23 in the small HB1 (Fig. 6A). The bulky adamantyl groups bind to V25 in the larger HB2 (Figs. 2 and 6A), similar to ART (Fig. 2). The good structural fit of PAC and ETA to EP is also reflected in an improved ΔG_b relative to AMA, RIM, and memantine hydrochloride (MEM). While PAC and ETA are considerably smaller than ART, their EI values are comparable, suggesting that a simplified, well-aligned scaffold can outperform larger, more complex molecules.

The experimental antiviral activities of PAC and ETA were tested against SARS-CoV-2 for the first time in this study, and the results are shown in Fig. 6. Earlier, PAC was synthesized and tested against the influenza A virus [85]. ETA was previously synthesized as a building block for a series of hypoxia-inducible factor 1 inhibitors [86]. We found that ETA exhibits one order of magnitude higher antiviral activity (EC_{50} = 10.13 μM; Fig. 6B) against the delta variant than AMA, MEM, and RIM (EC_{50} = 300 to 400 μM; Table S3). PAC (EC_{50} = 7.78 μM; Fig. 6B) outperforms every other compound in the previous part of the present study (AMA, MEM, RIM, ART, and ETA with EC_{50} = 40 to 400 μM; Table S3) against the omicron variant.

The selectivity index (SI = CC_{50}/EC_{50}) was also calculated to express the practical applicability of the investigated compounds. All 4 FDA-approved AMS drugs (gray in Fig. 1B) have a maximum SI of 4.55 for the delta, omicron, and Wuhan variants (Table S3). The laboratory measurements verified that the SI of PAC improved for the delta, omicron (SI = 11.18; Table S3), and Wuhan (SI = 18.01; Table S3) variants over all 4 FDA-approved AMS drugs. All in all, PAC shows a successful improvement in

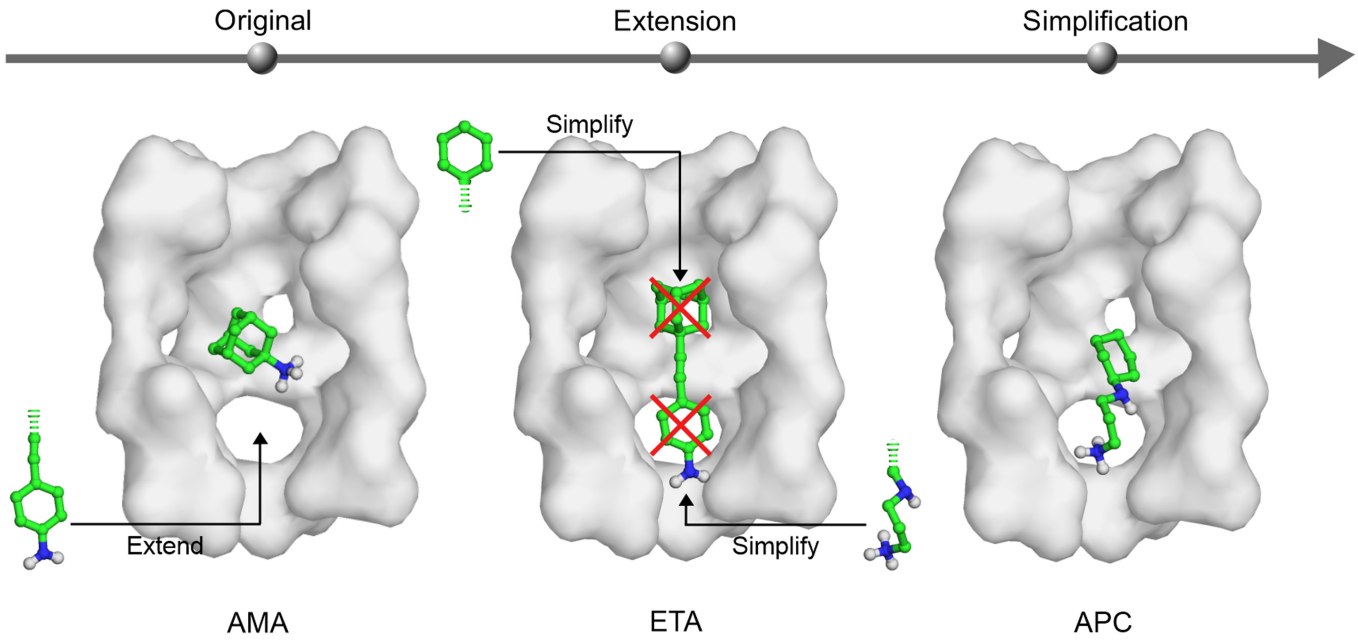

Fig. 5. The scaffold redesign strategy, including extension and simplification, resulting in the transformations from AMA to ETA to APC in the AMS series. Water molecules are omitted for clarity, but they are included in the detailed figures. The adamantyl group of AMA is depicted in a space-filling model, and the new groups added during the redesign are shown in ball-and-stick models.

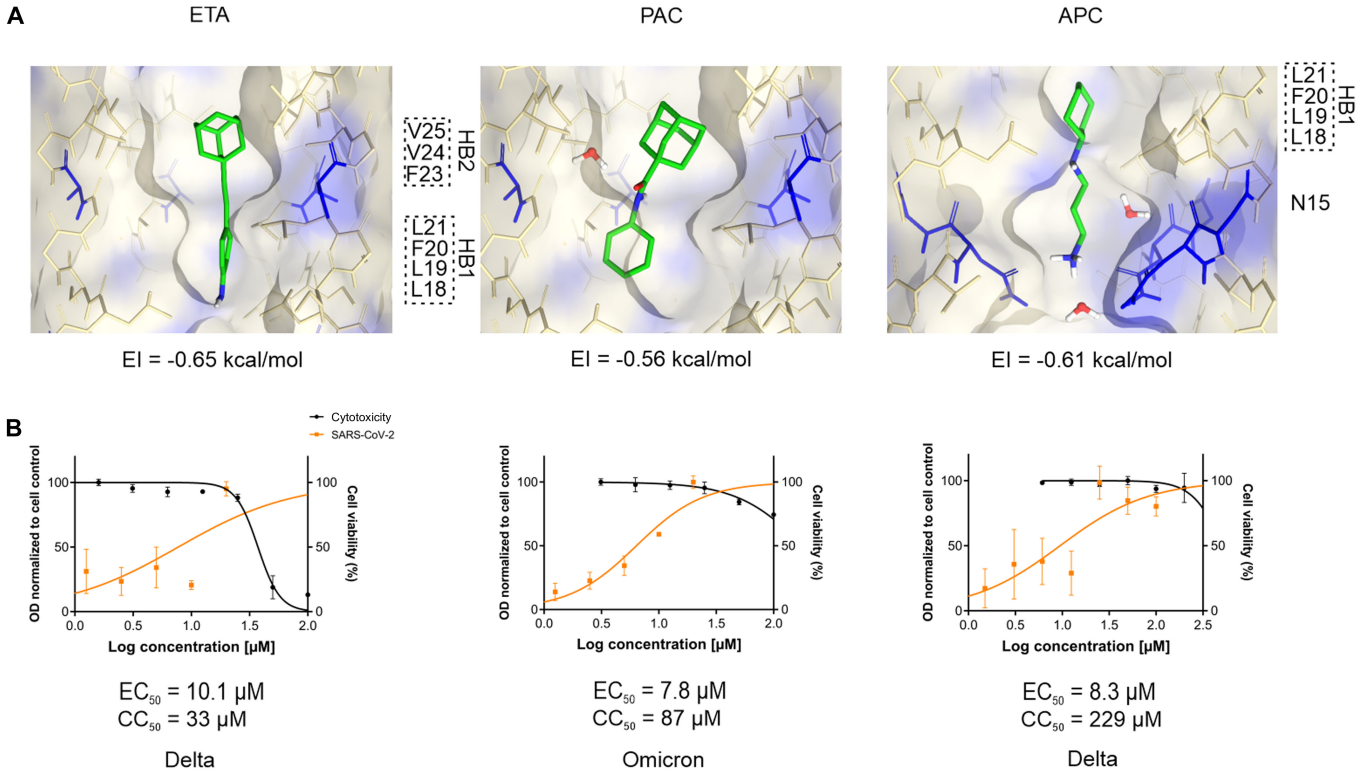

Fig. 6. Top results of the simplified scaffold redesign strategy from this study. (A) The binding modes of ETA, PAC, and APC to EP as produced by HydroDock. EP is shown as a surface, while ETA, PAC, and APC are represented as green sticks; water molecules are depicted as white and red balls and sticks. The blue and tan bands indicate hydrophilic and hydrophobic regions, respectively, based on the chemical properties of the amino acid residues lining the internal wall of EP. The bottom of the figure points toward the extraviral space. (B) The results from virology and cytology laboratory (MTT assay) tests of ETA, PAC, and APC. The orange curves indicate the inhibitory effects on SARS-CoV-2 replication, and the black curves show the cytotoxicity measurements. The concentration–response curves were generated from a representative biological experiment, in which each concentration was measured in 3 technical replicates. Error bars indicate the standard deviation of the technical replicates.

both activity (Fig. 6B) and SI (Table S3) as a top result of scaffold extension informed by SAR insights from Step 1.

Simplification of the scaffold

Despite the improvements observed for the compounds with extended scaffold (PAC and ETA; see the previous section), the high synthetic cost of the advanced C(sp^3)–H functionalization [68] of their adamantyl precursors still limits their usefulness. To enhance synthetic accessibility and maintain (or improve) SI and antiviral activity, the adamantyl scaffold was simplified to either a phenyl or a cyclohexyl group (Fig. 5), the simplest alternatives to the adamantyl group.

Based on the phenyl ring, 4-*tert*-butylcyclohexylamine (BCA; Fig. 1B), *trans*-4-boc-aminocyclohexylamine (BOC; Fig. 1B), and 3-methoxytyramine (MOX; Fig. 1B) were investigated. Between the hydrophobic moiety and the amino group, there are 2 atoms in MOX, and no atoms in BCA and BOC. The antiviral potential of these compounds against SARS-CoV-2 is reported here for the first time. The laboratory experiments demonstrate that BCA is highly cytotoxic; therefore, it was not tested for antiviral activity. MOX and BOC are not cytotoxic; however, they are ineffective against SARS-CoV-2 *in vitro* (as expected, since their binding modes do not align with the hydrophobic/hydrophilic regions of EP).

The simplification of the adamantyl scaffold to a cyclohexyl group yielded *N*-(3-aminopropyl)cyclohexylamine (APC; Fig. 1B). The binding mode of APC to EP was calculated using HydroDock (Fig. 6A). In the 4-atom linker between the cyclohexane ring and the terminal amino group of APC, there is an imino group (Fig. 1B), which can interact with the backbone carboxyl of N15 below the HB1 of EP (Fig. 6A). The 3-carbon alkyl linker of APC provides sufficient space for the amino group to interact with the N15 side chain and a water molecule below HB1 (Fig. 6A). The cyclohexyl ring interacts with the side chains of L18 and L21 in HB1, similar to the adamantane scaffold of the base compound AMA (Fig. 5). Consequently, the corresponding parts of APC align well with the hydrophilic and hydrophobic regions of EP, similar to PAC or ETA (Step 3). The calculated EI of APC is more favorable than that of ART and PAC (Table S1), indicating that APC is a promising candidate for further laboratory testing.

In a previous study, APC was tested against malaria [87], but not against viruses. Our laboratory results confirmed that APC has low cytotoxicity (Table S3 and Fig. 6B) and is highly effective against SARS-CoV-2 *in vitro* (Table S3). Among all tested compounds, APC shows the most potent antiviral activity against the delta strain (EC_{50} = 8.32 μM; Fig. 6 and Table S3) and exhibits antiviral activity comparable to ART against the omicron and Wuhan strains (EC_{50} = 49.42 and 8.16 μM, respectively; Table S3). The SI of APC exceeds 28 and 27 against the Wuhan and delta strains, representing 9- and 6-fold improvements, respectively, over the corresponding SI values of ART (Table S3). APC was comparably potent in immunofluorescence assays (Table S4 and Fig. S7) as in MTT assays.

Since APC is a much simpler compound than others with adamantyl-based AMS (Fig. 1B), it provides a synthetically more feasible and still active scaffold for the future design of potent antivirals targeting ion channels.

Conclusions

Common high-throughput screening [3] and drug repositioning have many limitations in antiviral drug research [17,88]. Instead, in the present study, we redesigned the antiviral scaffold through a 4-step target-based engineering approach. In Step 1, SARs were derived using a combination of computational methods, HydroDock [29] and QMH-L [69], which can handle water molecules [29,89] and electronic effects during the prediction of binding affinity. As a laboratory test system (Step 2), we targeted multiple SARS-CoV-2 variants encoding a conserved ion channel (EP), which has strong potential as a drug target. Based on the SARs, we designed an extended AMS (Step 3), resulting in an improved fit within the ion channel and the identification of 2 new compounds. Finally, the simplification (Step 4) yielded a cyclohexylamine-based minimalist scaffold in APC with good synthetic accessibility. Substantial improvements were achieved with APC over FDA-approved drugs in terms of efficiency (the most potent EC_{50} = 8.32 μM against the delta strain) and safety (the highest SI of 28.06 against the Wuhan strain). Since the geometry and alternating hydrophobic pattern are standard features of ion channels in various viruses, the final, simplified scaffold will serve as an excellent starting point for antiviral drug design.

Materials and Methods

Molecular engineering

Calculation of ligand binding modes

The HydroDock [29] protocol was applied to produce the hydrated target–ligand complexes of AMS bound EP. The M2 and EP bound AMA and RIM structures were used from our previous study [29]. The atomic coordinates of EP were acquired from the Protein Data Bank [90] under the accession code 7k3g [32]. The N- and C-terminal ends of the protein were capped in Maestro [91] by adding acetyl- and imino-methyl groups to mimic the backbone of the protein [92]. Polar hydrogen atoms and Gasteiger-Marsili partial charges were added in AutoDockTools [93]. MEM, ART, PAC, ETA, MOX, APC, BOC, and BCA were built in Maestro, and energy minimized with OpenBabel [94]. The parameter files of the compounds for the molecular dynamics (MD) simulations were prepared using the CHARMM-GUI [95].

Dry docking of the compounds to EP was performed in AutoDock 4.2.6. A total of 100 blind docking runs were performed, and the docking box covered the entire surface of the protein. Flexibility was allowed on the ligand side; the Lamarckian genetic algorithm was used. The ligand binding modes were clustered and ranked based on their calculated free energy of binding values.

The hydrated target file was used from our previous study [29]. In the third step of the HydroDock protocol, the first-ranked, dry-docked binding modes were merged with the hydrated target files. If the first-ranked, dry-docked binding mode was outside the channel, then the first-ranked binding mode was used, which is inside the channel.

Minimization and MD of the complex

Overlapping water molecules with the ligands were removed with MobyWat [96]. The resulting hydrated target–dry docked ligand complex structures were subject to a 5-step energy minimization [29]. The system was solvated in explicit TIP3P water molecules, and counterions were added to achieve neutrality. First, a steepest descent and a conjugate gradient minimization were carried out, followed by a 100-ps MD simulation and a second steepest descent and conjugate gradient minimization, exactly as in Ref. [29]. The resulting systems were ready for MD

simulations lasting up to 100 ns. AMBER [97] force field was used during MD simulations. The temperature was coupled to a constant of 303.15K. The pressure was coupled to a constant of 1 bar. Particle Mesh-Ewald summation was used for long-range electrostatics. Van der Waals and Coulomb interactions were cut off at 11 Å. Position restraints were applied to the Cα atoms of the target protein. The final trajectory containing all atomic coordinates of all frames was converted to a portable XDR binary file. The representative structure of each simulation was selected as the closest match to the statistical average of all ligand frames, as in Ref. [29]. There was one exception, in the case of APC, where the frame with the most favorable calculated interaction energy (E_{inter}, see the next section) was selected. The binding mode of the energetically most favorable and the representative frames was similar.

E_{inter} energy calculation

The energy of the representative binding modes was calculated, including water molecules within 3.5 Å distance from the ligand, and these water molecules were treated as part of the target. Lennard–Jones and Coulomb (Mehler–Solmajer [98]) interaction energies were calculated as in Eqs. (1) and (2). The AMBER parameter files were used from the MD simulations, besides the atomic coordinates as input files for energy calculation.

$$E_{\text{inter}} = E_{\text{LJ}} + E_{\text{Coulomb}} = \sum_{i,j}^{N_E N_S} \left(\frac{A_{ij}}{r_{ij}^{12}} - \frac{B_{ij}}{r_{ij}^{6}} + \frac{q_i q_j}{4\pi\varepsilon_0 \varepsilon_r r_{ij}} \right)$$
$$A_{ij} = \varepsilon_{ij} R_{ij}^{12}$$
$$B_{ij} = 2\varepsilon_{ij} R_{ij}^{6} \quad (1)$$
$$R_{ij} = R_i + R_j$$
$$\varepsilon_{ij} = \sqrt{\varepsilon_i \varepsilon_j}$$

$$\varepsilon_r = A + \frac{B}{1 + ke^{-\lambda B r}} \quad (2)$$

E_{inter} is the sum of Lennard–Jones (LJ) and Coulomb (Cb) intermolecular interaction energies [Eq. (1)]. The Coulomb term was calculated with a distance-dependent dielectric function [Eq. (2)] In Eq. (1), ε_{ij} is the potential well depth at equilibrium between the ith (ligand) and jth (protein) atoms; ε_0 is the permittivity of vacuum; ε_r is the relative permittivity [Eq. (2)]; R_{ij} is the inter-nuclear distance at equilibrium between the ith (ligand) and jth (protein) atoms; q is the partial charge of an atom; r_{ij} is the actual distance between the ith (ligand) and jth (protein) atoms; NE is the number of protein atoms; NS is the number of ligand atoms. In Eq. (2), $B = \varepsilon_0 - A$, ε_0 is the dielectric constant of water at 25 °C, and A, λ, and k are parameters.

ΔG_b calculation

For the representative frames, a quantum mechanics-based change in free energy of binding (ΔG_b) was calculated using the QMH-L method as described in Ref. [69]. Briefly, the water molecules within 3.5 Å distance from both target and ligand were kept, and the heat of formation ($\Delta_f H$) of the hydrated target–ligand complex, the dry target, and the dry ligand was calculated using MOPAC [99] quantum chemistry software. According to Hess' law [Eqs. (3) and (4)], the $\Delta_f H$ of the target, the ligand, and the water molecules (−65.2 kcal/mol multiplied by the number of water molecules) were subtracted from the $\Delta_f H$ of the complex, resulting in a calculated heat of reaction ($\Delta_r H$) as described in Ref. [69]. Then, the number of heavy atoms was divided by the number of atoms to result in the NHA/NA descriptor necessary for the calculation of ΔG_b according to Eq. (5) [69]). The calculated ΔG_b values are shown in Table S1.

$$\text{Target}\left[H_2O\right]_x + \text{ligand}\left[H_2O\right]_y + z\ H_2O = \text{target: ligand}\left[H_2O\right]_{x+y+z} \quad (3)$$

$$\Delta_r H = \Delta_f H\left(\text{target: ligand}\left[H_2O\right]_{x+y+z}\right) - \Delta_f H\left(\text{target}\left[H_2O\right]_x\right) - \Delta_f H\left(\text{ligand}\left[H_2O\right]_y\right) - z\ \Delta_f H\left(H_2O\right) \quad (4)$$

$$\Delta G_b = 1.26 \times 10^{-2} \Delta_r H - 30.93 \times \text{NHA}/\text{NA} + 9.25 \quad (5)$$

Chemical syntheses

While the synthesis of PAC and ETA has been previously documented in the literature [85,86], we also achieved a substantial reduction in reaction times by using one-pot syntheses and microwave-assisted conditions (Sonogashira coupling yielded a notable increase in ETA yield), in line with green chemistry principles. Thus, PAC and ETA are simpler extensions of AMA, providing an easily synthesizable scaffold for AMS alternative to the expensive, complicated ART.

N-phenyladamantane-1-carboxamide

1-Adamantanecarbonyl chloride (199 mg, 1.00 mmol), acetanilide (135 mg, 1.00 mmol), and toluene (3 ml) were added to a 10-ml microwave vessel under a nitrogen atmosphere. The mixture was heated in a microwave reactor at 130 °C for 20 min under stirring. After cooling to room temperature, the solvent was evaporated *in vacuo*, and the residue was purified by flash chromatography with 20% ethyl acetate/80% hexane as eluent. Compound PAC (Fig. 7) was identical to the compound described in the literature [85].

4-(Adamantan-1-ylethynyl)aniline

4-Iodoaniline (219 mg, 1.00 mmol), $PdCl_2(PPh_3)_2$ (70 mg, 0.1 mmol), CuI (19 mg, 0.1 mmol), and *N*,*N*-dimethylformamide (DMF) (3 ml) were added under nitrogen atmosphere, then Et_3N (0.84 ml, 6 mmol) was added and the mixture was stirred at 40 °C for 10 min in a 10-ml microwave vessel. 1-Ethynyladamantane (160 mg, 1.00 mmol) was added, and the mixture was heated in a microwave reactor at 40 °C for 30 min under stirring. The solvent was evaporated *in vacuo*. The residue was purified by flash chromatography with 20% ethyl acetate/80% hexane as eluent. Compound ETA (Fig. 7) was identical to the compound described in the literature [86].

Chemical analyses

Thin-layer chromatography was performed on silica gel 60 F254 (layer thickness, 0.2 mm; Merck). The spots were detected with I_2 or UV (365 nm). Flash chromatography was performed on silica gel 60, 40 to 63 μm (Merck). Reactions under microwave irradiation were carried out in the Anton Paar Monowave 400

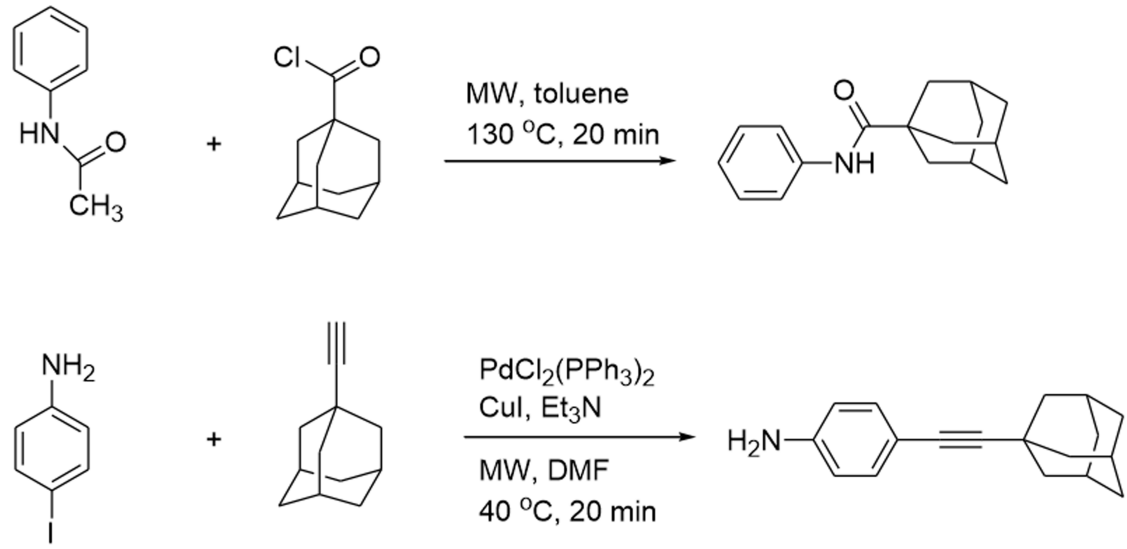

Fig. 7. Synthesis of PAC (top) and ETA (bottom).

microwave reactor. ^{1}H NMR spectra were recorded in dimethyl sulfoxide (DMSO)-d_6 solution with a Bruker DRX-500 instrument at 500 MHz. ^{13}C NMR spectra (Figs. S5 and S6) were recorded with the same instrument at 125 MHz under the same conditions.

PAC

Compound PAC was obtained as a white solid (232 mg, 91%). Anal calcd. for $C_{17}H_{21}NO$: C, 79.96; H, 8.29. Found: C, 80.05; H, 8.34. Mr: 255.35. ^{1}H NMR (500 MHz, DMSO-d_6) δ ppm: 1.71 (broad s, 6H), 1.90 (overlapping signals, 6H), 2.02 (broad s, 3H), 7.02 (t, 1H, J = 7.4 Hz), 7.27 (t, 2H, J = 7.4 Hz), 7.64 (d, 2H, J = 7.4 Hz), 9.07 (s, 1H, NH); ^{13}C NMR (125 MHz, DMSO-d_6) δ ppm: 27.6 (3C, 3xCH), 35.9 (3C, 3xCH_2), 38.2 (3C, 3xCH_2), 40.8 (C), 120.1 (2C, 2xCH), 123.0 (CH), 128.2 (2C, 2xCH), 139.2 (C), 175.8 (C).

ETA

Compound ETA was obtained as a white solid (224 mg, 89%). Anal calcd. for $C_{18}H_{21}N$: C, 86.01; H, 8.42. Found: C, 86.09; H, 8.47. Mr: 251.37. ^{1}H NMR (500 MHz, DMSO-d_6) δ ppm: 1.67 (s, 6H), 1.86 (overlapping signals, 6H), 1.94 (s, 3H), 5.32 (s, 2H, NH_2), 6.46 (d, 2H, J = 7.4 Hz), 6.97 (d, 2H, J = 7.4 Hz); ^{13}C NMR (DMSO-d_6) δ ppm: 27.3 (3C, 3xCH), 29.4 (C), 35.7 (3C, 3xCH_2), 42.7 (3C, 3xCH_2), 80.2 and 94.6 (C≡CH), 109.4 (C), 113.4 (2C, 2xCH), 132.1 (2C, 2xCH), 148.3 (C).

Virology and cytology laboratory measurements

Cell lines and virus strains

Vero E6 cells (African Green Monkey renal epithelial cells; ATCC cat. no. CRL-1586) were maintained in Dulbecco's Modified Eagle Medium (DMEM) (Lonza, Basel, Switzerland) supplemented with 10% heat-inactivated fetal bovine serum (FBS) (Gibco, Waltham, MA, USA), and 1% penicillin–streptomycin (Pen/Strep; Lonza, Basel, Switzerland) at 37 °C and 5% CO_2 in a humidified atmosphere. The Vero E6 cell line can be infected with SARS-CoV-2 [100] and the study was performed with different variants of SARS-CoV-2: P.2—mentioned later as Wuhan variant; B.1.617—hereinafter referred as delta variant; B.1.1.529—mentioned later as omicron variant; and B.1.1.7.—referred to as the alpha variant. The experiments were performed in a BSL-4 laboratory.

Reagent preparation

AMA (97% purity), MEM (98% purity), and 1-(1-adamantyl)ethylamine-hydrochloride, also called RIM (99% purity, racemic), were purchased from Merck (Darmstadt, Germany). ART (98% purity), MOX (98.36% purity), and APC (99,37% purity) were purchased from MedChemExpress (USA). BOC (97% purity) and BCA were purchased from Thermo Fisher Scientific (USA). AMA, MEM, RIM, ART, MOX, APC, BOC, BCA, PAC, and ETA were solubilized in sterile water or DMSO, and 10 mM stocks were made of them. The drugs were further diluted with medium to reach working concentrations.

Cytotoxicity assay

To determine the cytotoxicity of test drugs, an MTT cell viability assay was performed, and cell cytotoxicity was examined with Cell Proliferation Kit I (Roche, Switzerland). The MTT assay is a quick colorimetric method to assess the viability of cells by measuring their metabolic activity. Viable cells convert MTT to formazan via cellular oxidoreductases, leading to a color change measured by spectrophotometry (absorbance). During the cytotoxicity test, VeroE6 cells were seeded into a 96-well tissue culture plate at a density of 3×10^4 cells per well and were incubated overnight. After that, cells were treated with compounds diluted at the indicated concentrations.

RIM and MEM were used at 7 different concentrations ranging from 100 to 400 μM. AMA was used at 6 different concentrations ranging from 150 to 800 μM. ART, MOX, APC, BOC, BCA, PAC, and ETA were used at 14 different concentrations ranging from 3 to 600 μM. The different concentration values were selected based on the preliminary microscopically observed toxicity values (data not mentioned in the manuscript). After 72 h of treatment, cells were washed with DMEM, and MTT Labeling reagent was added. After 4 h incubation at 37 °C, the Solubilization solution was added and incubated overnight. The absorbance of formazan was measured at 570 nm with the Crocodile 5-in-1 mini Workstation (Berthold, Germany). The CC_{50} values were calculated using GraphPad Prism version

8.00 software (GraphPad Software, San Diego, CA, USA) using nonlinear regression. Three technical replicates of each concentration were used. Three biological replicates of the positive and negative controls were used. The SI was calculated by dividing the EC_{50} (calculated as described below) by the CC_{50}.

The use of cytotoxicity tests was important to find out the concentration of the drugs that do not cause cell death, but their concentration is high enough to inhibit virus replication.

Cytopathic effect inhibition assay

Antiviral assays were performed under BSL-4 conditions, and viral stocks were prepared as previously described [100]. Antiviral activity was initially assessed in independent biological screening experiments to verify the reproducibility of the observed effects. The concentration–response curves presented in the manuscript were generated from a representative biological experiment, in which each concentration was measured in 3 technical replicates. Error bars indicate the standard deviation of the technical replicates.

To test the effect of drugs on virus replication, Vero E6 cells were seeded into 96-well plates at a density of 3×10^4 cells per well the day before the antiviral experiment. Cells were treated with the test compounds at different concentrations (previously described). Immediately after treatment, cells were infected with different variants of SARS-CoV-2 at a multiplicity of infection (MOI) of 0.5. MOI is the ratio of agents to infection targets. Cells were incubated for 30 min at 37 °C, then the supernatant was replaced with fresh maintenance media (DMEM, 2% FBS, and 1% Pen/Strep) supplemented with the compounds at the appropriate concentration. After 72 h of treatment, virus-induced cytopathic effects (CPE) were microscopically examined (data not mentioned in the manuscript), cells were washed with DMEM, and MTT Labeling reagent was added. After 4 h incubation at 37 °C, the Solubilization solution was added and incubated overnight. The absorbance of formazan was measured at 570 nm with the Crocodile 5-in-1 mini Workstation (Berthold, Germany). The EC_{50} was calculated using GraphPad Prism version 8.00 software (GraphPad Software, San Diego, CA, USA) for nonlinear regression. Three biological replicates of each concentration were used. Treatment plates included biological replicates of the positive and negative controls; infected/nontreated and noninfected/nontreated controls were used. Briefly, noninfected and untreated cells were used as negative controls to define baseline cell viability, whereas infected and untreated cells served as positive controls representing the maximum virus-induced cytopathic effect. These controls were included in each experimental run and were used for normalization of the assay data.

Immunofluorescence assay

Cells were fixed with ice-cold methanol for 30 min and blocked with 1% bovine serum albumin (Thermo Fisher Scientific) in phosphate-buffered saline (PBS). Cells were then incubated with a mouse monoclonal anti-double-stranded RNA (dsRNA) antibody (clone K1; Invitrogen, Thermo Fisher Scientific, catalog no. 10020200-200UG, 1:1,000) for 1 h at 37 °C, followed by incubation with Goat Anti-Mouse IgG (H+L) Alexa Fluor 488 secondary antibody (Abcam, catalog no. ab150113, 1:1,000) for 30 min at 37 °C. Finally, nuclei were stained with DAPI (4′,6-diamidino-2-phenylindole) solution (1 mg/ml; Thermo Fisher Scientific, catalog no. 62248) for 10 min at room temperature. Cells were washed 5 times with PBS between each incubation step. Fluorescence images were acquired using an ImageXpress Pico Automated Cell Imaging System (Molecular Devices, San Jose, CA, USA) equipped with a 10× objective. Nine nonoverlapping fields of view were acquired per well using identical acquisition settings for all samples. Image analysis was performed using CellReporterXpress software (Molecular Devices) to determine the total number of cells and the number of infected (dsRNA-positive) cells. Data from 3 technical replicate wells were analyzed for each experimental condition. The percentage of infected cells was calculated and used for quantitative analysis.

Microscopy

Vero E6 cells were seeded on a 96-well plate; infected with variants, as alpha, omicron, and delta variants at an MOI of 0.5; and treated with ART in parallel with infection. The images (Fig. 4) were taken with Omni, a live-cell analysis platform.

Statistical analysis

Sigmoidal concentration–response curves were fitted, and EC_{50} values and plots were generated using GraphPad Prism version 8.00 software (GraphPad Software, San Diego, CA, USA).

Acknowledgments

The manuscript is dedicated to the memory of Prof. Dr. Ferenc Jakab. We acknowledge the Digital Government Development and Project Management Ltd. for awarding us access to the Komondor HPC facility based in Hungary.

Funding: This paper was supported by the János Bolyai Research Scholarship of the Hungarian Academy of Sciences. The work was supported by the National Research, Development and Innovation Office (PharmaLab, RRF-2.3.1-21-2022-00015). This work was also supported by the National Research, Development and Innovation Office-NKFIH through project SNN 139323. The project no. TKP-2021-EGA-13 was implemented with support from the National Research, Development, and Innovation Fund of Hungary, financed under the TKP2021-EGA funding scheme.

Author contributions: B.Z.Z. and C.H. elaborated the strategy, designed theoretical calculations, interpreted the data, and wrote the manuscript. C.H. supervised the project. E.M. synthesized compounds and wrote the corresponding part of the manuscript. F.F., Z.K., K.L., M.M., B.Z., and A.K. performed laboratory experiments and wrote the corresponding part of the manuscript. B.Z.Z. and C.H. acquired funding.

Competing interests: The authors declare that they have no competing interests.

Data Availability

The authors declare that all the data supporting the findings of this study are available within the paper and the Supplementary Materials, which are deposited at https://zenodo.org/records/21296129.

Supplementary Materials

Figs. S1 to S7
Tables S1 to S4

References

1. De Rycker M, Baragaña B, Duce SL, Gilbert IH. Challenges and recent progress in drug discovery for tropical diseases. *Nature*. 2018;559(7715):498–506.

2. Irwin KK, Renzette N, Kowalik TF, Jensen JD. Antiviral drug resistance as an adaptive process. *Virus Evol*. 2016;2(1): Article vew014.
3. Yu Y, Li Z, Guo R, Qian J, Zhang H, Zhang J, Zhao X, Wang S, Wang Y. Ononin, sec-O-β-d-glucosylhamaudol and astragaloside I: Antiviral lead compounds identified via high throughput screening and biological validation from traditional Chinese medicine Zhongjing formulary. *Pharmacol Res*. 2019;145:Article 104248.
4. Pertea M, Salzberg SL. Between a chicken and a grape: Estimating the number of human genes. *Genome Biol*. 2010;11(5):206.
5. Takashita E. Influenza polymerase inhibitors: Mechanisms of action and resistance. *Cold Spring Harb Perspect Med*. 2021;11(5):Article a038687.
6. Kausar S, Said Khan F, Ishaq Mujeeb Ur Rehman M, Akram M, Riaz M, Rasool G, Hamid Khan A, Saleem I, Shamim S, Malik A. A review: Mechanism of action of antiviral drugs. *Int J Immunopathol Pharmacol*. 2021;35:Article 20587384211002621.
7. Zhu Y, Yurgelonis I, Noell S, Yang Q, Guan S, Li Z, Hao L, Rothan H, Rai DK, McMonagle P, et al. In vitro selection and analysis of SARS-CoV-2 nirmatrelvir resistance mutations contributing to clinical virus resistance surveillance. *Sci Adv*. 2024;10(30):Article eadl4013.
8. Chatterjee S, Bhattacharya M, Dhama K, Lee S-S, Chakraborty C. Resistance to nirmatrelvir due to mutations in the Mpro in the subvariants of SARS-CoV-2 omicron: Another concern? *Mol Ther Nucleic Acids*. 2023;32:263–266.
9. Padhi AK, Tripathi T. Hotspot residues and resistance mutations in the nirmatrelvir-binding site of SARS-CoV-2 main protease: Design, identification, and correlation with globally circulating viral genomes. *Biochem Biophys Res Commun*. 2022;629:54–60.
10. Strasfeld L, Chou S. Antiviral drug resistance: Mechanisms and clinical implications. *Infect Dis Clin North Am*. 2010;24(2):413–437.
11. Aw DZH, Zhang DX, Vignuzzi M. Strategies and efforts in circumventing the emergence of antiviral resistance against conventional antivirals. *NPJ Antimicrob Resist*. 2025;3(1):54.
12. Wang H. Practical updates in clinical antiviral resistance testing. *J Clin Microbiol*. 2024;62(8):Article e0072823.
13. De Jesús-González LA, León-Juárez M, Lira-Hernández FI, Rivas-Santiago B, Velázquez-Cervantes MA, Méndez-Delgado IM, Macías-Guerrero DI, Hernández-Castillo J, Hernández-Rodríguez X, Calderón-Sandate DN, et al. Advances and challenges in antiviral development for respiratory viruses. *Pathogens*. 2024;14(1):20.
14. Westberg M, Su Y, Zou X, Huang P, Rustagi A, Garhyan J, Patel PB, Fernandez D, Wu Y, Hao C, et al. An orally bioavailable SARS-CoV-2 main protease inhibitor exhibits improved affinity and reduced sensitivity to mutations. *Sci Transl Med*. 2024;16(738):Article eadi0979.
15. Soares VC, Moreira IBG, Dias SSG. SARS-CoV-2 infection and antiviral strategies: Advances and limitations. *Viruses*. 2025;17(8):1064.
16. Owen DR, Allerton CMN, Anderson AS, Aschenbrenner L, Avery M, Berritt S, Boras B, Cardin RD, Carlo A, Coffman KJ, et al. An oral SARS-CoV-2 M^{pro} inhibitor clinical candidate for the treatment of COVID-19. *Science*. 2021;374(6575): 1586–1593.
17. Charness ME, Gupta K, Stack G, Strymish J, Adams E, Lindy DC, Mohri H, Ho DD. Rebound of SARS-CoV-2 infection after nirmatrelvir–ritonavir treatment. *N Engl J Med*. 2022;387(11):1045–1047.
18. Iketani S, Mohri H, Culbertson B, Hong SJ, Duan Y, Luck MI, Annavajhala MK, Guo Y, Sheng Z, Uhlemann A-C, et al. Multiple pathways for SARS-CoV-2 resistance to nirmatrelvir. *Nature*. 2023;613(7944):558–564.
19. Kiso M, Furusawa Y, Uraki R, Imai M, Yamayoshi S, Kawaoka Y. In vitro and in vivo characterization of SARS-CoV-2 strains resistant to nirmatrelvir. *Nat Commun*. 2023;14(1):3952.
20. Lo C-W, Kariv O, Hao C, Gammeltoft KA, Bukh J, Gottwein J, Westberg M, Lin MZ, Einav S. Replication capacity and susceptibility of nirmatrelvir-resistant mutants to next-generation Mpro inhibitors in a SARS-CoV-2 replicon system. *Antiviral Res*. 2024;231:Article 106022.
21. Yaghi RM, Wylie DC, Andrews CL, Dickert OH, Ram A, Iverson BL. An investigation of nirmatrelvir (Paxlovid) resistance in SARS-CoV-2 M^{pro}. *ACS Bio Med Chem Au*. 2024;4(6):280–290.
22. Liu Z, VanBlargan LA, Bloyet L-M, Rothlauf PW, Chen RE, Stumpf S, Zhao H, Errico JM, Theel ES, Liebeskind MJ, et al. Identification of SARS-CoV-2 spike mutations that attenuate monoclonal and serum antibody neutralization. *Cell Host Microbe*. 2021;29(3):477–488.e4.
23. Singh A, Arkin IT. Targeting viral ion channels: A promising strategy to curb SARS-CoV-2. *Pharmaceuticals*. 2022;15(4):396.
24. Russell T, Gangotia D, Barry G. Assessing the potential of repurposing ion channel inhibitors to treat emerging viral diseases and the role of this host factor in virus replication. *Biomed Pharmacother*. 2022;156:Article 113850.
25. Schlicksup CJ, Zlotnick A. Viral structural proteins as targets for antivirals. *Curr Opin Virol*. 2020;45:43–50.
26. Bianchi M, Borsetti A, Ciccozzi M, Pascarella S. SARS-Cov-2 ORF3a: Mutability and function. *Int J Biol Macromol*. 2021;170:820–826.
27. Issa E, Merhi G, Panossian B, Salloum T, Tokajian S. SARS-CoV-2 and ORF3a: Nonsynonymous mutations, functional domains, and viral pathogenesis. *mSystems*. 2020;5(3): Article e00266-20.
28. Benazraf A, Arkin IT. Exhaustive mutational analysis of severe acute respiratory syndrome coronavirus 2 ORF3a: An essential component in the pathogen's infectivity cycle. *Protein Sci*. 2023;32(1):Article e4528.
29. Zsidó BZ, Börzsei R, Szél V, Hetényi C. Determination of ligand binding modes in hydrated viral ion channels to foster drug design and repositioning. *J Chem Inf Model*. 2021;61(8):4011–4022.
30. Thomaston JL, Polizzi NF, Konstantinidi A, Wang J, Kolocouris A, DeGrado WF. Inhibitors of the M2 proton channel engage and disrupt transmembrane networks of hydrogen-bonded waters. *J Am Chem Soc*. 2018;140(45):15219–15226.
31. Liu J, Obando D, Liao V, Lifa T, Codd R. The many faces of the adamantyl group in drug design. *Eur J Med Chem*. 2011;46(6):1949–1963.
32. Mandala VS, McKay MJ, Shcherbakov AA, Dregni AJ, Kolocouris A, Hong M. Structure and drug binding of the SARS-CoV-2 envelope protein transmembrane domain in lipid bilayers. *Nat Struct Mol Biol*. 2020;27(12):1202–1208.

33. Magazine N, Zhang T, Wu Y, McGee MC, Veggiani G, Huang W. Mutations and evolution of the SARS-CoV-2 spike protein. *Viruses*. 2022;14(3):640.
34. Barrantes FJ. Structural biology of coronavirus ion channels. *Acta Crystallogr D Struct Biol*. 2021;77(Pt 4):391–402.
35. Wang Y, Pan X, Ji H, Zuo X, Xiao G-F, Li J, Zhang L-K, Xia B, Gao Z. Impact of SARS-CoV-2 envelope protein mutations on the pathogenicity of omicron XBB. *Cell Discov*. 2023;9(1):80.
36. Islam MA, Shahi S, Marzan AA, Amin MR, Hasan MN, Hoque MN, Ghosh A, Barua A, Khan A, Dhama K, et al. Variant-specific deleterious mutations in the SARS-CoV-2 genome reveal immune responses and potentials for prophylactic vaccine development. *Front Pharmacol*. 2023;14:Article 1090717.
37. Štimac A, Šekutor M, Mlinarić-Majerski K, Frkanec L, Frkanec R. Adamantane in drug delivery systems and surface recognition. *Molecules*. 2017;22(2):297.
38. Wanka L, Iqbal K, Schreiner PR. The lipophilic bullet hits the targets: Medicinal chemistry of adamantane derivatives. *Chem Rev*. 2013;113(5):3516–3604.
39. Wingfield WL, Pollack D, Grunert RR. Therapeutic efficacy of amantadine HCl and rimantadine HCl in naturally occurring influenza A2 respiratory illness in man. *N Engl J Med*. 1969;281(11):579–584.
40. Torres J, Maheswari U, Parthasarathy K, Ng L, Liu DX, Gong X. Conductance and amantadine binding of a pore formed by a lysine-flanked transmembrane domain of SARS coronavirus envelope protein. *Protein Sci*. 2007;16(9):2065–2071.
41. Kobe N, Dreisewerd L, Pavlin M, Kogovšek P, Podlipnik Č, Grošelj U, Lukšič M. *In silico* determination of novel SARS-CoV-2 envelope protein ion channel inhibitors. *Comput Struct Biotechnol J*. 2025;27:2823–2831.
42. Fink K, Nitsche A, Neumann M, Grossegesse M, Eisele K-H, Danysz W. Amantadine inhibits SARS-CoV-2 in vitro. *Viruses*. 2021;13(4):539.
43. Lim SY, Guo Z, Liu P, McKay LG, Storm N, Griffiths A, Qu MD, Finberg RW, Somasundaran M, Wang JP. Anti-SARS-CoV-2 activity of adamantanes in vitro and in animal models of infection. *COVID*. 2022;2(11):1551–1563.
44. Butterworth RF. Potential for the repurposing of adamantane antivirals for COVID-19. *Drugs R D*. 2021;21(3):267–272.
45. Toft-Bertelsen TL, Jeppesen MG, Tzortzini E, Xue K, Giller K, Becker S, Mujezinovic A, Bentzen BH, Andreas LB, Kolocouris A, et al. Amantadine inhibits known and novel ion channels encoded by SARS-CoV-2 in vitro. *Commun Biol*. 2021;4(1):1402.
46. Zhou Y, Gammeltoft KA, Galli A, Offersgaard A, Fahnøe U, Ramirez S, Bukh J, Gottwein JM. Efficacy of ion-channel inhibitors amantadine, memantine and rimantadine for the treatment of SARS-CoV-2 in vitro. *Viruses*. 2021;13(10):2082.
47. Sasaki-Tanaka R, Shibata T, Moriyama M, Okamoto H, Kogure H, Kanda T. Amantadine and rimantadine inhibit hepatitis A virus replication through the induction of autophagy. *J Virol*. 2022;96(18):Article e0064622.
48. Rejdak K, Fiedor P, Bonek R, Goch A, Gala-Błądzińska A, Chełstowski W, Łukasiak J, Kiciak S, Dąbrowski P, Dec M, et al. The use of amantadine in the prevention of progression and treatment of COVID-19 symptoms in patients infected with the SARS-CoV-2 virus (COV-PREVENT): Study rationale and design. *Contemp Clin Trials*. 2022;116:Article 106755.
49. Aranda-Abreu GE, Aranda-Martínez JD, Araújo R. Use of amantadine in a patient with SARS-CoV-2. *J Med Virol*. 2021;93(1):110–111.
50. Albert Cortés B. Protective effect of amantadine in a COVID-19 patient: Case report. *Res Rev Infect Dis*. 2020;3(2):100–101.
51. de Almeida Marques DP, Andrade LA, Reis EV, Clarindo FA, Moraes TD, Lourenço KL, De Barros WA, Costa NE, de Andrade LM, Lopes-Ribeiro Á, et al. New anti-SARS-CoV-2 aminoadamantane compounds as antiviral candidates for the treatment of COVID-19. *Virus Res*. 2024;340:Article 199291.
52. Harandi AA, Pakdaman H, Medghalchi A, Kimia N, Kazemian A, Siavoshi F, Barough SS, Esfandani A, Hosseini MH, Sobhanian SA. A randomized open-label clinical trial on the effect of amantadine on post Covid 19 fatigue. *Sci Rep*. 2024;14(1):1343.
53. Barczyk A, Czajkowska-Malinowska M, Farnik M, Barczyk M, Boda Ł, Cofta S, Duława J, Dyrbuś M, Harat R, Huk M, et al. Efficacy of oral amantadine among patients hospitalised with COVID-19: A randomised, double-blind, placebo-controlled, multicentre study. *Respir Med*. 2023;212:Article 107198.
54. Chober D, Czajkowski Z, Aksak-Wąs B, Dalewska-Kucharczyk K, Hołubczak K, Karasińska-Milchert S, Jaremko M, Skowron M, Karasińska-Cieślak M, Parczewski M. Improved survival in intensive care unit in severe COVID-19 associated with amantadine use—Retrospective study. *Int J Infect Dis*. 2022;124:143–151.
55. Singh Tomar PP, Arkin IT. SARS-CoV-2 E protein is a potential ion channel that can be inhibited by gliclazide and memantine. *Biochem Biophys Res Commun*. 2020;530(1):10–14.
56. Yu H-G, Sizemore G, Martinez I, Perrotta P. Inhibition of SARS-CoV-2 viral channel activity using FDA-approved channel modulators independent of variants. *Biomolecules*. 2022;12(11):1673.
57. Breitinger U, Ali NKM, Sticht H, Breitinger H-G. Inhibition of SARS CoV envelope protein by flavonoids and classical viroporin inhibitors. *Front Microbiol*. 2021;12:Article 692423.
58. Breitinger U, Sedky CA, Sticht H, Breitinger H-G. Patch-clamp studies and cell viability assays suggest a distinct site for viroporin inhibitors on the E protein of SARS-CoV-2. *Virol J*. 2023;20(1):142.
59. Negi V, Kuhn RJ. A BSL-2 chimeric system designed to screen SARS-CoV-2 E protein ion channel inhibitors. *J Virol*. 2025;99(5):Article e0225224.
60. Torres J, Pervushin K, Surya W. Prediction of conformational states in a coronavirus channel using Alphafold-2 and DeepMSA2: Strengths and limitations. *Comput Struct Biotechnol J*. 2024;23:3730–3740.
61. Vaidya H, Gautam S, Kumar M. Anti-EBV: Artificial intelligence driven predictive modeling for repurposing drugs as potential antivirals against Epstein-Barr virus. *Comput Struct Biotechnol J*. 2025;27:1784–1799.
62. Roterman I, Slupina M, Konieczny L. Protein folding: Funnel model revised. *Comput Struct Biotechnol J*. 2024;23:3827–3838.
63. Prete AL, Corradini BT, Costanti F, Scarselli F, Bianchini M. Leveraging molecular graphs for natural product classification. *Comput Struct Biotechnol J*. 2025;27:3837–3884.
64. Mee-udorn P, Narkpuk J, Jaru-ampornpan P, Hongeng S, Uengwetwanit T, Srimongkolpithak N. Repurposing of the nucleoside analogs for influenza. *Comput Struct Biotechnol J*. 2025;27:3762–3769.

65. Nagarajan SK, Weber J, Roderer D, Piontek J. *C. perfringens* enterotoxin-claudin pore complex: Models for structure, mechanism of pore assembly and cation permeability. *Comput Struct Biotechnol J*. 2025;27:287–306.
66. Catalina-Hernández È, López-Martín M, Masnou-Sánchez D, Martins M, Lorenz-Fonfria VA, Jiménez-Altayó F, Hellmich UA, Inada H, Alcaraz A, Furutani Y, et al. Experimental and computational biophysics to identify vasodilator drugs targeted at TRPV2 using agonists based on the probenecid scaffold. *Comput Struct Biotechnol J*. 2024;23:473–482.
67. Runfeng L, Yunlong H, Jicheng H, Weiqi P, Qinhai M, Yongxia S, Chufang L, Jin Z, Zhenhua J, Haiming J, et al. Lianhuaqingwen exerts anti-viral and anti-inflammatory activity against novel coronavirus (SARS-CoV-2). *Pharmacol Res*. 2020;156:Article 104761.
68. Dane C, Montgomery AP, Kassiou M. The adamantane scaffold: Beyond a lipophilic moiety. *Eur J Med Chem*. 2025;291:Article 117592.
69. Szél V, Zsidó BZ, Jeszenői N, Hetényi C. Target–ligand binding affinity from single point enthalpy calculation and elemental composition. *Phys Chem Chem Phys*. 2023;25(46):31714–31725.
70. Zsidó BZ, Hetényi C. Water in drug design: Pitfalls and good practices. *Expert Opin Drug Discov*. 2025;20(6):745–764.
71. Zsidó BZ, Hetényi C. The role of water in ligand binding. *Curr Opin Struct Biol*. 2021;67:1–8.
72. Hetényi C, Van Der Spoel D. Blind docking of drug-sized compounds to proteins with up to a thousand residues. *FEBS Lett*. 2006;580(5):1447–1450.
73. Kobe N, Dreisewerd L, Lukšič M, Pavlin M, Grošelj U, Podlipnik Č, Janc M, Lengar Ž, Mrak P, Žnidarič MT, et al. In silico characterisation of a novel SARS-CoV-2 envelope protein inhibitor and in vitro validation against murine coronavirus. *Bioorg Chem*. 2026;178:Article 109949.
74. Kairys V, Baranauskiene L, Kazlauskiene M, Zubrienė A, Petrauskas V, Matulis D, Kazlauskas E. Recent advances in computational and experimental protein-ligand affinity determination techniques. *Expert Opin Drug Discov*. 2024;19(6):649–670.
75. Ginex T, Vázquez J, Estarellas C, Luque FJ. Quantum mechanical-based strategies in drug discovery: Finding the pace to new challenges in drug design. *Curr Opin Struct Biol*. 2024;87:Article 102870.
76. Zsidó BZ, Bayarsaikhan B, Börzsei R, Szél V, Mohos V, Hetényi C. The advances and limitations of the determination and applications of water structure in molecular engineering. *Int J Mol Sci*. 2023;24(14):11784.
77. Hopkins AL, Groom CR, Alex A. Ligand efficiency: A useful metric for lead selection. *Drug Discov Today*. 2004;9(10):430–431.
78. Hopkins AL, Keserü GM, Leeson PD, Rees DC, Reynolds CH. The role of ligand efficiency metrics in drug discovery. *Nat Rev Drug Discov*. 2014;13(2):105–121.
79. Hamaluba M, van der Pluijm RW, Weya J, Njuguna P, Ngama M, Kalume P, Mwambingu G, Ngetsa C, Wambua J, Boga M, et al. Arterolane–piperaquine–mefloquine versus arterolane–piperaquine and artemether–lumefantrine in the treatment of uncomplicated *Plasmodium falciparum* malaria in Kenyan children: A single-centre, open-label, randomised, non-inferiority trial. *Lancet Infect Dis*. 2021;21(10):1395–1406.
80. Mosmann T. Rapid colorimetric assay for cellular growth and survival: Application to proliferation and cytotoxicity assays. *J Immunol Methods*. 1983;65(1–2):55–63.
81. Heldt CL, Hernandez R, Mudiganti U, Gurgel PV, Brown DT, Carbonell RG. A colorimetric assay for viral agents that produce cytopathic effects. *J Virol Methods*. 2006;135(1):56–65.
82. Ghosh AK, Miller H, Knox K, Kundu M, Henrickson KJ, Arav-Boger R. Inhibition of human coronaviruses by antimalarial peroxides. *ACS Infect Dis*. 2021;7(7):1985–1995.
83. Drakopoulos A, Tzitzoglaki C, McGuire K, Hoffmann A, Konstantinidi A, Kolokouris D, Ma C, Freudenberger K, Hutterer J, Gauglitz G, et al. Unraveling the binding, proton blockage, and inhibition of influenza M2 WT and S31N by rimantadine variants. *ACS Med Chem Lett*. 2018;9(3):198–203.
84. Forrestall K, Pringle ES, Sands D, Duguay BA, Farewell B, Woldemariam T, Falzarano D, Pottie I, McCormick C, Darvesh S. A phenothiazine urea derivative broadly inhibits coronavirus replication via viral protease inhibition. *Antiviral Res*. 2023;220:Article 105758.
85. Leiva R, Barniol-Xicota M, Codony S, Ginex T, Vanderlinden E, Montes M, Caffrey M, Luque FJ, Naesens L, Vázquez S. Aniline-based inhibitors of influenza H1N1 virus acting on hemagglutinin-mediated fusion. *J Med Chem*. 2018;61(1):98–118.
86. Nagao S, Yamane Y, Funasaka S, Tanaka K, Miyazaki K, Kotake Y, Kamata JI, Watanabe-Miyano S, Toyama O, Ozawa Y, et al. Synthesis and structure–activity relationships of novel, potent, orally active hypoxia-inducible factor-1 inhibitors. *Bioorg Med Chem*. 2014;22(19):5513–5529.
87. Burger PB, Williams M, Sprenger J, Reeksting SB, Botha M, Müller IB, Joubert F, Birkholtz L-M, Louw AI. A novel inhibitor of *Plasmodium falciparum* spermidine synthase: A twist in the tail. *Malar J*. 2015;14:54.
88. Cao B, Wang Y, Wen D, Liu W, Wang J, Fan G, Ruan L, Song B, Cai Y, Wei M, et al. A trial of lopinavir–ritonavir in adults hospitalized with severe Covid-19. *N Engl J Med*. 2020;382(19):1787–1799.
89. Szél V, Zsidó BZ, Hetényi C. Enthalpic classification of water molecules in target–ligand binding. *J Chem Inf Model*. 2024;64(16):6583–6595.
90. Berman HM, Battistuz T, Bhat TN, Bluhm WF, Bourne PE, Burkhardt K, Feng Z, Gilliland GL, Iype L, Jain S, et al. The Protein Data Bank. *Acta Crystallogr D Biol Crystallogr*. 2002;58(6):899–907.
91. Schrödinger Release 2024-1. Maestro. New York (NY): Schrödinger, LLC; 2024.
92. Bálint M, Horváth I, Mészáros N, Hetényi C. Towards unraveling the histone code by fragment blind docking. *Int J Mol Sci*. 2019;20(2):422.
93. Morris GM, Huey R, Lindstrom W, Sanner MF, Belew RK, Goodsell DS, Olson AJ. AutoDock4 and AutoDockTools4: Automated docking with selective receptor flexibility. *J Comput Chem*. 2009;30(16):2785–2791.
94. O'Boyle NM, Banck M, James CA, Morley C, Vandermeersch T, Hutchison GR. Open babel: An open chemical toolbox. *J Cheminform*. 2011;3:33.
95. Brooks BR, Brooks CL, Mackerell AD, Nilsson L, Petrella RJ, Roux B, Won Y, Archontis G, Bartels C, Boresch S, et al. CHARMM: Molecular dynamics simulation package. *J Comput Chem*. 2009;30(10):1545–1614.
96. Jeszenői N, Horváth I, Bálint M, Van Der Spoel D, Hetényi C. Mobility-based prediction of hydration structures of protein surfaces. *Bioinformatics*. 2015;31(12):1959–1965.

97. Wang J, Wolf RM, Caldwell JW, Kollman PA, Case DA. Development and testing of a general Amber force field. *J Comput Chem*. 2004;25(9):1157–1174.
98. Mehler EL, Solmajer T. Electrostatic effects in proteins: Comparison of dielectric and charge models. *Protein Eng Des Sel*. 1991;4(8):903–910.
99. Stewart JJ, Klamt A, Thiel W, Danovich D, Rocha GB, Gieseking RL, Moussa JE, Kurtz HA, Korambath P, Merz KM, et al. MOPAC (22.0.0). 2022. https://Doi.Org/10.5281/Zenodo.6511959
100. Ogando NS, Dalebout TJ, Zevenhoven-Dobbe JC, Limpens RWAL, van der Meer Y, Caly L, Druce J, de Vries JJC, Kikkert M, Bárcena M, et al. SARS-coronavirus-2 replication in Vero E6 cells: Replication kinetics, rapid adaptation and cytopathology. *J Gen Virol*. 2020;101(9):925–940.
101. Sayers EW, Beck J, Bolton EE, Brister JR, Chan J, Connor R, Feldgarden M, Fine AM, Funk K, Hoffman J, et al. Database resources of the National Center for Biotechnology Information in 2025. *Nucleic Acids Res*. 2025;53(D1):D20–D29.
102. Madeira F, Madhusoodanan N, Lee J, Eusebi A, Niewielska A, Tivey ARN, Lopez R, Butcher S. The EMBL-EBI job dispatcher sequence analysis tools framework in 2024. *Nucleic Acids Res*. 2024;52(W1):W521–W525.

Computational and Structural Biotechnology Journal

The Redesign of the Molecular Scaffold of Viral Ion Channel Blockers

Balázs Zoltán Zsidó, Erzsébet Mernyák, Zoltán Kopasz, Fanni Földes, Krisztina Leiner, Mónika Madai, Brigitta Zana, Anett Kuczmog, and Csaba Hetényi

Citation: Zsidó B, Mernyák E, Kopasz Z, Földes F, Leiner K, Madai M, Zana B, Kuczmog A, Hetényi C. The Redesign of the Molecular Scaffold of Viral Ion Channel Blockers. *Comput Struct Biotechnol J*. 2026;**35** (1):0188. DOI: 10.34133/csbj.0188

The rise of rapidly mutating viruses poses growing challenges for drug developers in the fight against antiviral resistance. Viral ion channels generally have low mutation rates and are therefore considered emerging targets for a sustainable solution to the problem of resistance. This study reports the redesign of scaffolds for drug candidates targeting viral ion channels. The redesign was powered by a combination of a computational docking protocol that accounts for water molecules (HydroDock) and a subsequent quantum mechanics-based scoring (QMH-L) of the drug candidates. Extending the antiviral amantadine led to new compounds that better match the alternating hydrophobic and hydrophilic patterns of the inner walls of ion channels—a common feature across many viruses. Simplifying the structure yielded a cyclohexylamine-based minimalist scaffold that demonstrates improved antiviral activity compared to other agents such as amantadine and arterolane. SARS-CoV-2 variants served as test systems in laboratory experiments. The new molecular scaffolds presented here provide a strong foundation for designing potent viral ion channel blockers, helping to fill the drug pipeline.
Image